ACS APPLIED MATERIALS & INTERFACES

Research Article

www.acsami.org

Dual-Functional CeO_2:Eu^{3+} Nanocrystals for Performance-Enhanced Dye-Sensitized Solar Cells

Jongmin Roh, Sun Hye Hwang, and Jyongsik Jang*

School of Chemical and Biological Engineering, College of Engineering, Seoul National University, 599 Gwanak-ro, Gwanak-gu, Seoul 151-742, Korea

Supporting Information

ABSTRACT: Single-crystalline, octahedral CeO_2:Eu^{3+} nanocrystals, successfully prepared using a simple hydrothermal method, were investigated to determine their photovoltaic properties in an effort to enhance the light-harvesting efficiency of dye-sensitized solar cells (DSSCs). The size of the CeO_2:Eu^{3+} nanocrystals (300−400 nm), as well as their mirrorlike facets, significantly improved the diffuse reflectance of visible light. Excitation of the CeO_2:Eu^{3+} nanocrystal with 330 nm ultraviolet light was re-emitted via downconversion photoluminescence (PL) from 570 to 672 nm, corresponding to the $^5D_0 \rightarrow {}^7F_J$ transition in the Eu^{3+} ions. Downconversion PL was dominant at 590 nm and had a maximum intensity for 1 mol % Eu^{3+}. The CeO_2:Eu^{3+} nanocrystal-based DSSCs exhibited a power conversion efficiency of 8.36%, an increase of 14%, compared with conventional TiO_2 nanoparticle-based DSSCs, because of the strong light-scattering and downconversion PL of the CeO_2:Eu^{3+} nanocrystals.

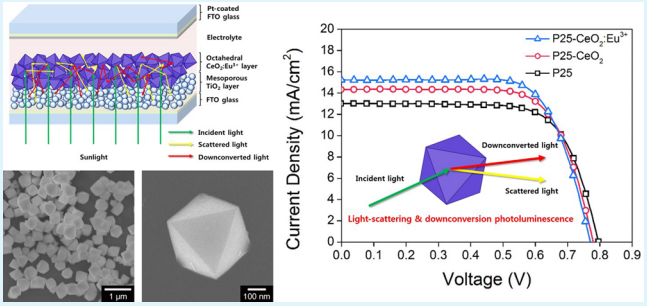

KEYWORDS: *CeO_2, CeO_2:Eu^{3+}, downconversion, dye-sensitized solar cell, europium, light-scattering, photoluminescence*

INTRODUCTION

As global demands for energy increase, photovoltaics have been recognized as a clean, renewable energy source. Since its introduction in 1991, the dye-sensitized solar cell (DSSC) is considered particularly promising, because of its low cost, easy production, and relatively high efficiency.[1−3] Conventional DSSC photoanodes are generally based on a mesoporous network of TiO_2 nanoparticles (NPs) upon which dye molecules are absorbed for light harvesting.[1,2,4] With light absorption, photoexcited electrons in the dyes are injected into the conduction band of the TiO_2 network.[4,5] From this viewpoint, the properties of the semiconductor materials and dyes in the photoanode have a direct effect on the efficiency of the DSSC. However, TiO_2 NPs give rise to a considerable loss of incident light due to the transmission of light through the photoanode.[6−8] Moreover, Ru-based dyes commonly used in DSSCs (e.g., N719, N749, and N3) have a narrow absorption spectral range in the visible regime, resulting in an energy loss of the incident light for ultraviolet (UV) and infrared (IR) wavelengths.[2,9] Therefore, high-performance DSSC photoanodes, capable of increasing light absorption and extending the light absorption range, are required to improve the existing conventional DSSC configuration.

An effective way to increase the light absorption capability of the photoanode is to introduce a scattering layer on top of the mesoporous TiO_2 layer. Large semiconductor microspheres (e.g., TiO_2,[6,8,10−13] ZnO,[14,15] SnO_2,[16,17] and CeO_2[18]),[13,19] hollow microspheres,[12,14,16,20] microplates,[11] and electrospun nanofibers[10,21] are utilized in the scattering layer to increase the optical path length of light. Among the semiconductor materials, CeO_2 offers an enhanced light-scattering ability for DSSCs, because of its cubic nanostructure with high refractive index for visible light and exposed mirrorlike facets.[22] Specifically, it is reported that the mirrorlike facets of CeO_2 significantly improve light scattering compared with curved surfaces, reflecting the incident light directly back to the photoanode.[18]

Another interesting approach for improving the performance of DSSCs is to broaden the light absorption range through downconversion phosphors.[23−28] Trivalent lanthanide ions (Ln^{3+}) are appropriate materials for downconversion, because of their abundant discrete energy levels, which allow them to convert UV light into visible light.[29] Europium ions (Eu^{3+}) are well-known as bright red luminescent phosphors and are commonly used as activators in various inorganic host lattices.[30] In particular, downconversion photoluminescence (PL) of Eu^{3+} ions have been examined in host materials Y_2O_3,[31] $NaGdF_4$,[32] Sr_2CeO_4,[33] and CeO_2.[34−36] In the downconversion process, the incident photon is converted into two or more low-energy photons, leading to high energy conversion efficiency in solar cells.[23] CeO_2:Eu^{3+} is a promising material for improving DSSC efficiency, exhibiting excellent downconversion luminescent properties through energy transfer from the Ce^{4+}−O^{2-} charge transfer transition in the CeO_2 host to the Eu^{3+} ions.[34]

Received: August 4, 2014
Accepted: October 24, 2014
Published: October 24, 2014

   dx.doi.org/10.1021/am505194k | ACS Appl. Mater. Interfaces 2014, 6, 19825−19832

Herein, we describe the dual functionality of CeO_2:Eu^{3+} nanocrystals, possessing both light-scattering and down-conversion luminescent properties. A CeO_2:Eu^{3+} layer was introduced to the TiO_2 layer of the photoanode in a DSSC device (Scheme 1). The as-synthesized CeO_2:Eu^{3+} nanocrystals

Scheme 1. Schematic Configuration of the Bilayer DSSC Device with Octahedral CeO_2:Eu^{3+} Nanocrystals for Light Scattering and Downconversion

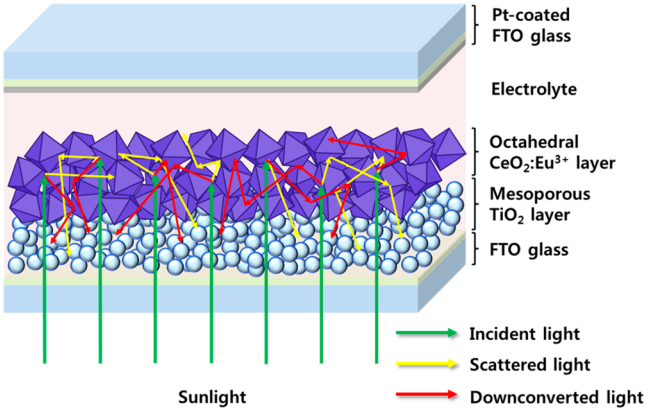

are large in size (300−400 nm) and have mirrorlike facets that facilitate light scattering. Additionally, the CeO_2:Eu^{3+} nanocrystals broadened the absorption range of the DSSC via downconversion luminescence, which in turn increased the photocurrent.

EXPERIMENTAL SECTION

1. Materials. Cerium(III) nitrate hexahydrate (99.99%) ($Ce(NO_3)_3{\cdot}6H_2O$), europium(III) nitrate pentahydrate (99.9%) ($Eu(NO_3)_3{\cdot}5H_2O$), trisodium phosphate dodecahydrate (98%) ($Na_3PO_4{\cdot}12H_2O$), lithium iodide, (crystalline powder, 99.9%) (LiI), iodine (99.99+%) (I_2), *tert*-butylpryidine (96%), acetonitrile (99.5%), and 2-propanol (99.9%) were obtained from Aldrich Chemical Co. (St. Louis, MO, USA). P25 TiO_2 NPs were purchased from Degussa (Germany). 3-Methyl-imidazolium iodide (BMII) and *cis*-diisothiocyanato-bis(2,20-bipyridyl-4,40-dicarboxylato) ruthenium(II) bis(tetrabutylammonium) (N719) were purchased from Solaronix (Aubonne, Switzerland). Fluorine-doped tin oxide (FTO) glass (sheet resistance: 15 Ω cm^{-2}; thickness: 2.2 mm) was obtained from Pilkington (Toledo, OH, USA).

2. Synthesis of CeO_2 and CeO_2:Eu^{3+} Nanocrystals. CeO_2 and CeO_2:Eu^{3+} nanocrystals were synthesized using a hydrothermal process. Typically, 2 g of cerium(III) nitrate hexahydrate, 0.02−0.4 g of europium(III) nitrate pentahydrate, and 7.6 mg of trisodium phosphate dodecahydrate were added to 80 mL of distilled water and stirred for 1 h. The mixture was then transferred to a 100 mL Teflon-lined stainless steel autoclave and heated at 180 °C for 12 h. Precipitates were collected by centrifugation, washed with water and ethanol, and then dried in an oven.

3. Cell Fabrication. The screen-printable P25 paste was prepared by adding ethyl cellulose, lauric acid, and terpineol to an ethanol solution of P25 particles, followed by stirring and sonication. The ethanol was removed using a rotary evaporator. The paste was then mixed using a 3-roll mill to create a homogeneous mixture. The nominal composition of P25/terpineol/ethyl cellulose/lauric acid was 1/3.3/0.5/0.3. FTO glass was cleaned by sonication in distilled water, acetone, and 2-propanol for 60 min each, followed by pretreatment with 40 mM $TiCl_4$ solution before being heated at 450 °C for 30 min. The P25 paste was coated onto the FTO glass by successive screen-printing. To prepare a CeO_2:Eu^{3+} dual-functional layer, the P25 paste with 20 wt % CeO_2:Eu^{3+} nanocrystals was mixed using a mortar and pestle. The mixed P25/CeO_2:Eu^{3+} paste was then screen-printed onto the P25 film, which was sintered at 450 °C for 30 min. The photoanode was then treated with 40 mM $TiCl_4$ and sintered at 450 °C for 30 min. The prepared films (area: 0.16 cm^2) were soaked in N719 dye solution (5×10^{-4} M in absolute ethanol) for 24 h and washed with absolute ethanol. Pt counter electrodes were prepared on the FTO glass using 5 mM H_2PtCl_6/2-propanol solution, followed by heating at 400 °C for 30 min. The washed working electrode was assembled with the Pt-coated counter electrode into a sandwich-type cell and sealed with 60 μm Surlyn. Then I^-/I^{3-} electrolyte containing 0.60 M BMII, 0.1 M LiI, 0.05 M I_2, and 0.5 M *tert*-butylpyridine in acetonitrile was injected into the cell.

4. Characterization. The morphology of the CeO_2 and CeO_2:Eu^{3+} nanocrystals was observed by energy-filtering transmission electron microscopy (EF-TEM, Carl Zeiss LIBRA 120), high-resolution transmission electron microscopy (HR-TEM), and selected-area electron diffraction (SAED) (JEOL JEM-3010). Field-emission scanning electron microscopy (FE-SEM) and energy-dispersive X-ray spectroscopy (EDS) data were obtained with a JEOL 6700. X-ray diffraction (XRD) was performed using a Bruker New D8 Advance with a Cu−Kα radiation source (λ: 1.5406 Å) at 40 kV and 300 mA (12 kW). X-ray photoelectron spectroscopy (XPS) was carried out with a SIGMA PROVE (ThermoVG). A Lambda 35 (PerkinElmer) UV−vis spectrometer was used for absorption measurements and diffuse reflectance spectroscopy (DRS). The band gap energy can be determined the plot of Kubelka−Munk fuction, $[F(R)h\nu]^{1/2} = A(h\nu - E_g)$ versus incident photon energy. $F(R)$ is the optical absorption coefficient which is calculated using reflectance data, $F(R) = (1 - R)^2/2R$. E_g is the band gap energy and A is the constant depending on transition probability.[37] All PL spectra were measured on a JASCO FP-6500 spectrofluorometer. The PL intensity of excitation/emission was investigated with increasing Eu^{3+} content over the wavelength ranges of 200−450 nm (λ_{ex} = 590 nm) and 550−700 nm (λ_{ex} = 330 nm). The photocurrent−voltage (I−V) characteristics of the assembled DSSCs were evaluated using a 530 W xenon lamp (XIL model 05A50KS source units; AM 1.5 solar irradiance; intensity: 100 mW cm^{-2}). The incident photon-to-current efficiency (IPCE, PV Measurements, Inc.) was measured from 300 to 800 nm under short-circuit conditions. EIS measurement was performed under a light illumination of 100 mW cm^{-2} using a Zahner Electrik IM6 analyzer. The applied bias voltage and ac amplitude were set at the open circuit voltage of DSSCs and 10 mV between the FTO/Pt counter electrode and the FTO/TiO_2/dye working electrode, respectively. The frequency range was explored from 10 mHz to 1 Hz. The impedance spectra were analyzed using an equivalent circuit model.[38]

RESULTS AND DISCUSSION

CeO_2:Eu^{3+} nanocrystals were synthesized by a simple hydrothermal process with slight modification. $Ce(NO_3)_3$ was used as the precursor to CeO_2 nanocrystals; $Eu(NO_3)_3$ was used as the Eu^{3+} dopant. Na_3PO_4, a mineralizer, played a prominent role in the development of the octahedral morphology of the CeO_2:Eu^{3+} nanocrystals.[39] $Ce(NO_3)_3$ and $Eu(NO_3)_3$ were dissolved in distilled water. Na_3PO_4 was then added to the aqueous solution to generate OH^- ions via hydrolysis. Ce^{3+} ions were further oxidized by O_2 in the aqueous system. The hydrated Ce^{4+} and Eu^{3+} ions formed complexes with the H_2O molecules or OH^- ions, taking the form of $Ce(H_2O)_x(OH^-)_y^{(4-y)+}$ and $Eu(H_2O)_x(OH^-)_y^{(3-y)+}$. In the hydrothermal process, polar H_2O molecules in the solution took protons away from the coordinated hydroxides in Ce^{4+} or Eu^{3+} complexes, resulting in the formation of CeO_2:Eu^{3+} nanocrystals.[40] The Eu^{3+} concentration in CeO_2:Eu^{3+} nanocrystals was adjusted by controlling the amount of $Eu(NO_3)_3$. The amount of Eu^{3+} in CeO_2:Eu^{3+} nanocrystals was confirmed by EDS analysis (see Table S1 in the Supporting Information), ranging from 0.1 to 2 mol %.

The morphology of the synthesized CeO_2:Eu^{3+} nanocrystals was investigated via TEM and SEM observation. Figure 1a, b

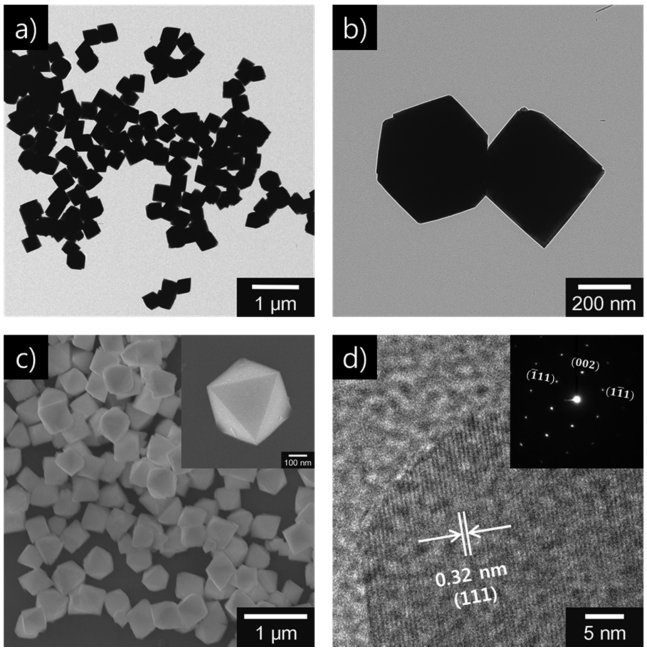

Figure 1. (a, b) TEM images, (c) SEM image, and (d) HR-TEM image of CeO_2:Eu^{3+} nanocrystals (1 mol % Eu^{3+}). The inset is a SAED pattern of CeO_2:Eu^{3+} nanocrystals.

show TEM images of CeO_2:Eu^{3+} nanocrystals. Figure 1c shows FE-SEM images of CeO_2:Eu^{3+} nanocrystals with 1 mol % Eu^{3+}. The fabricated CeO_2:Eu^{3+} nanocrystals had an octahedral structure with well-defined corners, edges, and mirrorlike facets, corresponding to the {111} plane of CeO_2 (Figure 1a–c). The size of the CeO_2:Eu^{3+} nanocrystals ranged from 300–400 nm. The HR-TEM image in Figure 1d revealed that the CeO_2:Eu^{3+} nanocrystals had well-developed two-dimensional (2D) lattice planes and good crystallinity. The *d*-spacing of 0.32 nm was well matched with the {111} plane of face-centered CeO_2. The SAED pattern of the CeO_2:Eu^{3+} nanocrystals corresponded to the $(\bar{1}11)$, (002), and $(1\bar{1}1)$ planes of single-crystalline CeO_2; thus, the structure of the CeO_2:Eu^{3+} nanocrystals was assigned to face-centered CeO_2, consistent with HR-TEM analysis. Compared with pristine CeO_2 nanocrystals, the Eu^{3+} ions did not influence the morphology of the CeO_2:Eu^{3+} nanocrystals with increasing Eu^{3+} content (see Figure S1 in the Supporting Information).

The crystallinity of the CeO_2:Eu^{3+} nanocrystals was confirmed by the XRD patterns (Figure 2a). The diffraction peaks of the CeO_2 and CeO_2:Eu^{3+} nanocrystals were identical and corresponded exactly to the (111), (200), (220), (311), (222), (400), (331), and (420) planes of pure cubic fluorite CeO_2. In addition, the peaks of Eu, Eu_2O_3, and $Eu(OH)_3$ were not observed in the CeO_2:Eu^{3+} nanocrystals. Considering the SAED and XRD patterns, these results suggest that the Eu^{3+} ions entered the CeO_2 lattices during the hydrothermal process and substituted for the Ce^{4+} ions without changing the cubic fluorite CeO_2 structure.

XPS analysis was carried out to identify the presence of Eu^{3+} ions in CeO_2:Eu^{3+} nanocrystals (Figure 2b). The peaks at 916.9 and 898.5 eV were assigned to the Ce^{4+} $3d_{3/2}$ and Ce^{4+} $3d_{5/2}$ contributions. The peaks centered at 901.2 and 882.6 eV

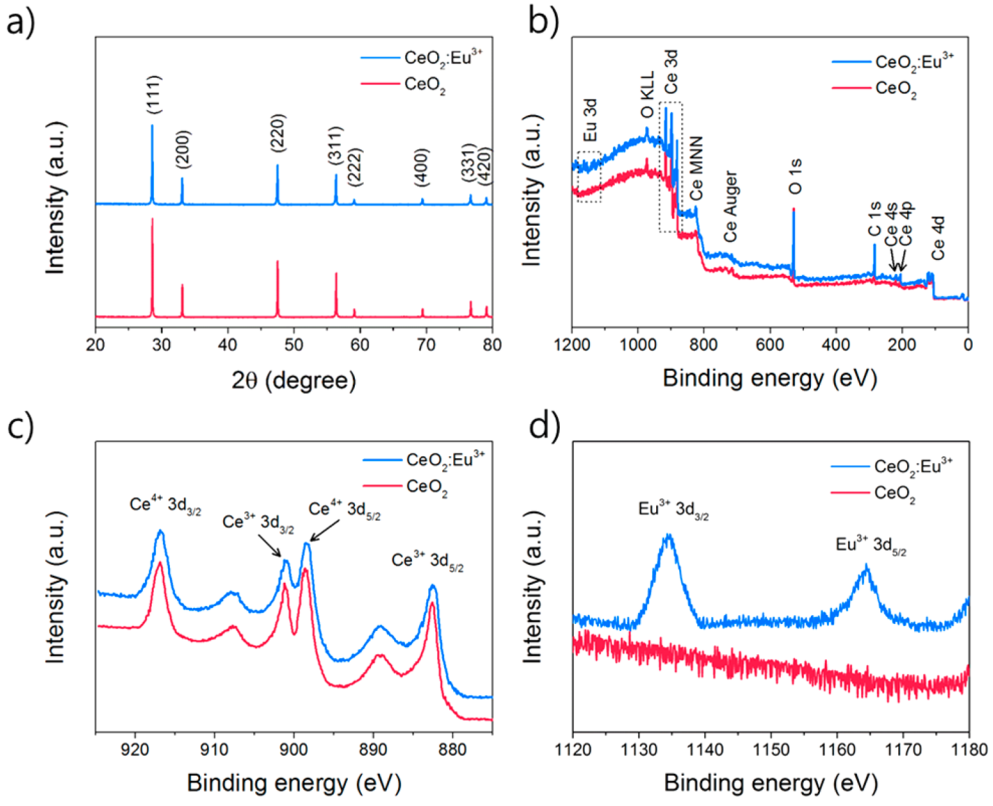

Figure 2. (a) XRD patterns of CeO_2 and CeO_2:Eu^{3+} nanocrystals (1 mol % Eu^{3+}), and XPS analysis showing (b) a full scan, (c) Ce 3d, and (d) the Eu 3d regions of CeO_2:Eu^{3+} nanocrystals.

corresponded to the binding energy of Ce^{3+} $3d_{3/2}$ and Ce^{3+} $3d_{5/2}$, which indicates that a small amount of Ce^{3+} was present on the CeO_2 surface. The existence of a small amount of Ce^{3+} at the surface of CeO_2 is well-known; moreover, the fraction of Ce^{3+} ions increases with decreasing particle size.[41] The peaks at 1164.2 and 1134.5 eV corresponded to the binding energy of Eu^{3+} $3d_{3/2}$ and Eu^{3+} $3d_{5/2}$, which indicated that europium ions in the CeO_2 lattices existed in the form of trivalent ions (Eu^{3+}). These results suggest that the CeO_2:Eu^{3+} nanocrystals possess europium ions in the Eu^{3+} form, as well as a small portion of Ce^{3+} ions.

To investigate the light-scattering ability of CeO_2:Eu^{3+} nanocrystals, we performed UV−vis DRS over the wavelength range of 300−800 nm (Figure 3a). The thicknesses of the pristine P25 film, CeO_2-incorporated P25 film, and CeO_2:Eu^{3+}-incorporated P25 film were adjusted to 10 μm. The diffuse reflectance of the CeO_2 and CeO_2:Eu^{3+} films was >60% in the range of 400−800 nm (Figure 3a), much higher than that of the pure P25 film. This improvement in the diffuse reflectance was attributed to effective light scattering by the large size and mirrorlike facets of the octahedral CeO_2 and CeO_2:Eu^{3+} nanocrystals. These mirrorlike facets increased the optical path length of the incident light by reflecting the incident light directly back to the TiO_2 films, resulting in enhancement of the photocurrent density in the DSSC.[42] The band gap energy (E_g) of the P25 film, P25+CeO_2 film and the P25+CeO_2:Eu^{3+} film can be determined by Kubelka−Munk transformation of diffuse reflectance data. Figure 3b shows the Kubelka−Munk plot for the P25 film, P25+CeO_2 (20 wt %) film and the P25+CeO_2:Eu^{3+} film (20 wt %, 1 mol % Eu^{3+}). From the extrapolation of the linear part of Kubelka−Munk plot, E_g for P25 film, P25+CeO_2 film and the P25+CeO_2:Eu^{3+} film are determined to be 3.11, 2.98, and 2.94 eV, respectively. Therefore, E_g of the P25+CeO_2:Eu^{3+} film are narrower than those of P25+CeO_2 film and the P25+CeO_2:Eu^{3+} film, which is indicated a better response in the visible region of the solar spectrum.

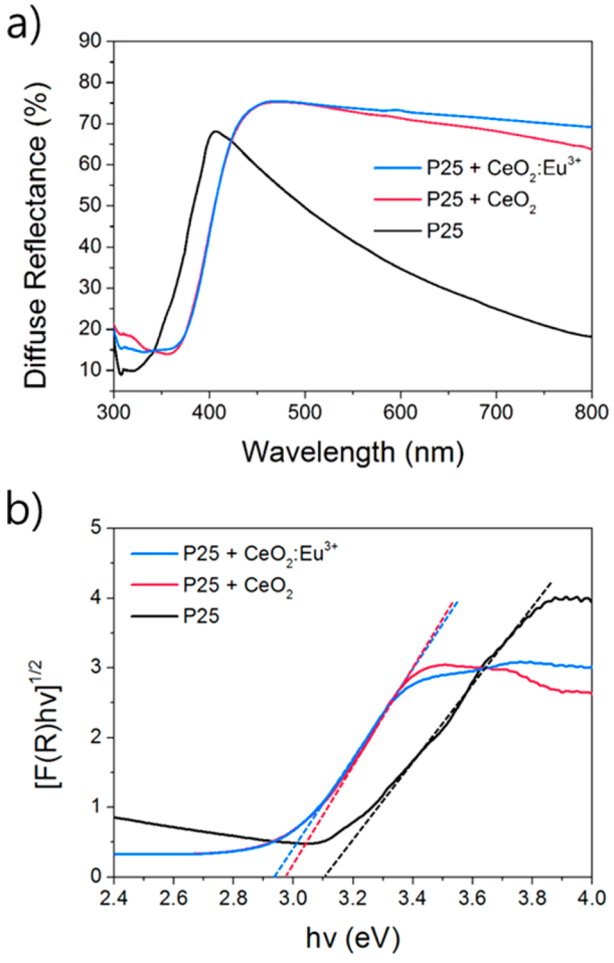

Figure 3. (a) UV−vis DRS and (b) transformed Kubelka−Munk spectra of a pristine P25 film, a P25+CeO_2 (20 wt %) film, and a P25+CeO_2:Eu^{3+} film (20 wt %, 1 mol % Eu^{3+}).

The downconversion PL properties were investigated by measuring the PL spectra of CeO_2:Eu^{3+} nanocrystals. Figure 4a shows the excitation spectra of CeO_2:Eu^{3+} nanocrystals with increasing Eu^{3+} concentration (0.1−2 mol % Eu^{3+}). All excitation spectra of the CeO_2:Eu^{3+} nanocrystals have broad bands with a maximum at 330 nm, which is attributed to the excitation of the host CeO_2 nanocrystals. The intensity of the excitation bands increased with increasing concentration of Eu^{3+} dopant and reached a maximum at 1 mol % Eu^{3+}. With a further increase in the Eu^{3+} concentration, the excitation intensity decreased due to concentration quenching of Eu^{3+} emission caused by cross-relaxation and energy migration among Eu^{3+} ions.[43]

Figure 4b shows the PL emission spectra of CeO_2:Eu^{3+} nanocrystals excited at 330 nm. The typical Eu^{3+} emission peaks at 570, 590, 610, 631, 650, and 672 nm were observed in all CeO_2:Eu^{3+} nanocrystals; these peaks were assigned to the $^5D_0 \rightarrow {}^7F_J$ (J = 0−4) transitions of Eu^{3+} ions, as follows: $^5D_0 \rightarrow {}^7F_0$ (570 nm), $^5D_0 \rightarrow {}^7F_1$ (590 nm), $^5D_0 \rightarrow {}^7F_2$ (610 and 631 nm), $^5D_0 \rightarrow {}^7F_3$ (650 nm), and $^5D_0 \rightarrow {}^7F_4$ (672 nm). It is known that the $^5D_0 \rightarrow {}^7F_1$ transition is a magnetic dipole transition that is insensitive to the crystal field strength around the Eu^{3+} ions, whereas the $^5D_0 \rightarrow {}^7F_2$ transition is hypersensitive to the local symmetry around the Eu^{3+} ions because of the electric dipole transition of $^5D_0 \rightarrow {}^7F_2$.[28] For this reason, when the Eu^{3+} ions are located in the CeO_2 lattice with an inversion symmetry, the $^5D_0 \rightarrow {}^7F_1$ transition dominates the emission spectrum. On the other hand, when the Eu^{3+} ions are positioned at sites without inversion symmetry, the $^5D_0 \rightarrow {}^7F_2$ transition dominates the emission spectrum and its intensity increases with increasing lattice distortion around the Eu^{3+} ions.[44] In Figure 4b, the $^5D_0 \rightarrow {}^7F_1$ transition at 590 nm is a dominant peak in the emission spectra of CeO_2:Eu^{3+} nanocrystals. This result suggests that the Eu^{3+} ions are located in CeO_2 lattices that possess inversion symmetry and that the structure of the CeO_2 lattices is maintained with increasing Eu^{3+} concentration in CeO_2:Eu^{3+} nanocrystals. The intensity of the $^5D_0 \rightarrow {}^7F_1$ transition increased gradually up to 1 mol % Eu^{3+}, followed by a decrease in the luminescence intensity with further increase in the Eu^{3+} concentration (i.e., concentration quenching). Together, these findings indicate that the host CeO_2 nanocrystals absorbed the UV light and transferred energy to the Eu^{3+} ions in CeO_2 nonradiatively. The Eu^{3+} ions then re-emitted the transferred energy as visible light via downconversion PL corresponding to the $^5D_0 \rightarrow {}^7F_J$ transition.

To confirm the possibility of using this PL effect in DSSCs, the emission spectra for CeO_2:Eu^{3+} nanocrystals were investigated before and after the addition of the D719 dye. Figure 4c shows the emission spectra of bare CeO_2:Eu^{3+} nanocrystals and CeO_2:Eu^{3+} nanocrystals with N719 dye. In contrast to that of bare CeO_2:Eu^{3+} nanocrystals, the emission

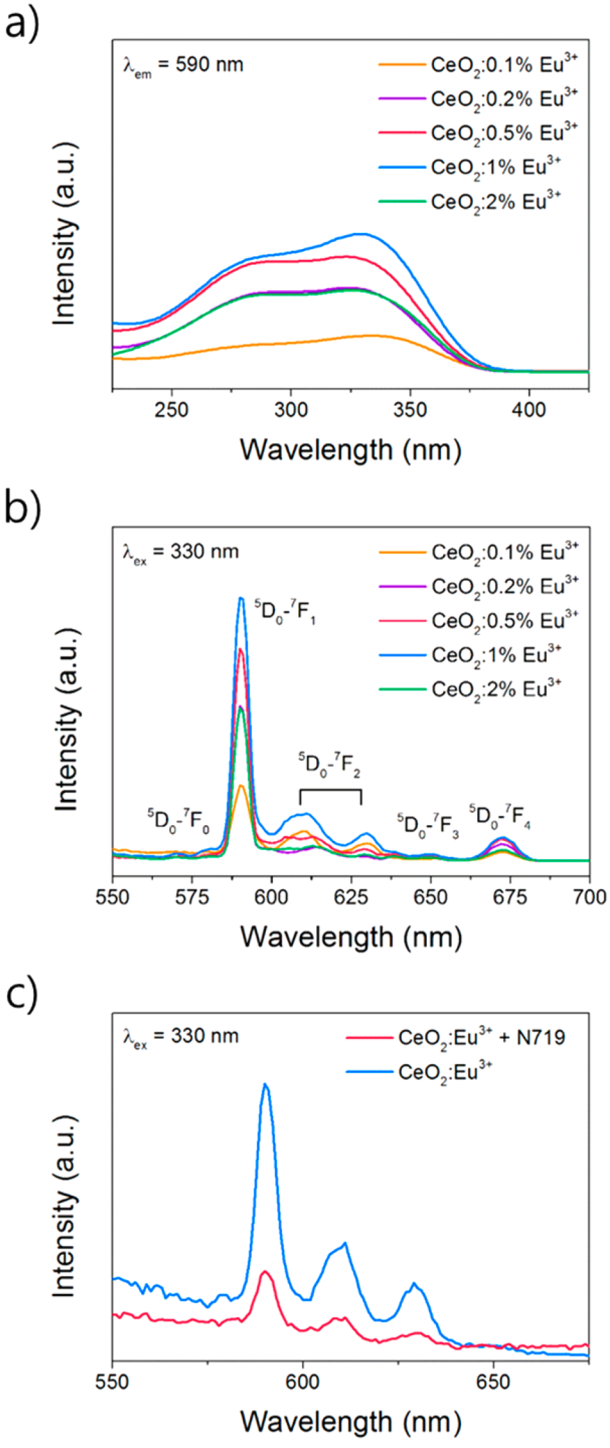

Figure 4. (a) Excitation and (b) emission spectra of the CeO_2:Eu^{3+} nanocrystals for various Eu^{3+} concentrations (0.1–2 mol %). (c) Emission spectra of CeO_2:Eu^{3+} nanocrystals (1 mol % Eu^{3+}), with and without N719 dye.

spectrum intensity of CeO_2:Eu^{3+} nanocrystals with N719 dye decreased significantly. This decrease in the emission intensity was attributed to emission quenching of the emitted PL because of absorption by the N719 dye surrounding the CeO_2:Eu^{3+} nanocrystals. Thus, UV light can be utilized in DSSCs to improve photocurrent and power conversion performance via N719 absorption of the downconversion PL of CeO_2:Eu^{3+} nanocrystals.

Bilayer DSSC devices, with a CeO_2 or CeO_2:Eu^{3+} layer on a P25 control film, were assembled to evaluate the light-scattering and downconversion effect on photovoltaic performance (Scheme 1). P25-CeO_2 and P25-CeO_2:Eu^{3+} photoanodes were prepared by successive screen-printing with the mixed P25-CeO_2:Eu^{3+} paste onto P25 reference photoanodes. The surface morphology and cross-section of the assembled DSSC photoanodes are given in Figure 5. The photocurrent density–

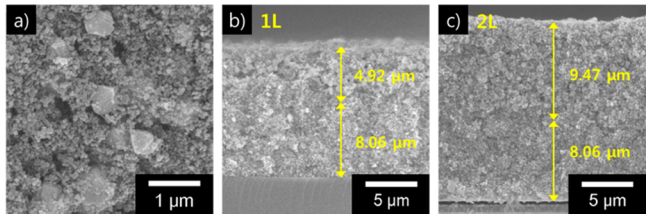

Figure 5. SEM image of (a) surface morphology and cross-sectional structure of P25-CeO_2:Eu^{3+} photoanode with (b) 1 layer and c) 2 layers.

voltage (J–V) curves of the P25, P25-CeO_2, and P25-CeO_2:Eu^{3+} photoanodes are shown in Figure 6a, and their photovoltaic properties are summarized in Table 1. The DSSC with the P25 control photoanode exhibited a short-circuit current density (J_{sc}) of 14.04 mA cm^{-2} and a power conversion efficiency (η) of 7.33%. With the CeO_2 layer added to the P25 photoanode, J_{sc} and η increased to 14.33 mA cm^{-2} and 7.92%, leading to an 8.08% enhancement in efficiency compared with the P25 reference cell. This enhancement was attributed to the increase in the optical path length of light resulting from the excellent light-scattering effect of CeO_2 nanocrystals. The effects of Eu^{3+} concentration in CeO_2:Eu^{3+} nanocrystals on the efficiency are shown in Figure 6c, and the photovoltaic properties are listed in Table S2 in the Supporting Information. The DSSCs with a CeO_2:Eu^{3+} layer exhibited a slightly enhanced J_{sc} and η, compared with the DSSC with a CeO_2 layer (see Table S2 in the Supporting Information). With increasing Eu^{3+} concentration in the CeO_2:Eu^{3+} nanocrystals, J_{sc} and η increased up to 1 mol %, followed by a decrease in J_{sc} and η with further increase in the Eu^{3+} concentration (Figure 6c). The best performance was obtained using a P25-CeO_2:Eu^{3+} photoanode with an Eu^{3+} concentration of 1 mol %, demonstrating J_{sc} and η values of 15.26 mA cm^{-2} and 8.36%, respectively. These results corresponded to a 5.49% enhancement in performance, compared with that of the P25-CeO_2 photoanode. This remarkable enhancement in J_{sc} and η was attributed to the downconversion luminescence properties of CeO_2:Eu^{3+} nanocrystals from UV to visible light, which can be absorbed and utilized by the N719 dye. However, when the Eu^{3+} concentration in CeO_2:Eu^{3+} nanocrystals exceeded 1 mol %, a decrease in J_{sc} was observed. This result may be associated with a decrease in the downconversion luminescence intensity by concentration quenching. The effect of CeO_2:Eu^{3+} layer thickness on the efficiency are shown in Figure S3 in the Supporting Information and their photovoltaic performances are summarized in Table S3 in the Supporting Information. Both J_{sc} and V_{oc} decreased with increasing the thickness of CeO_2:Eu^{3+} layer. The thick film has larger surface area compared with thin film and provides the additional charge recombination sites.[45] In addition, CeO_2 owns intrinsic oxygen vacancies, which can result in electron–hole recombination.[46] When Eu^{3+} concentration increases gradually, the effects of

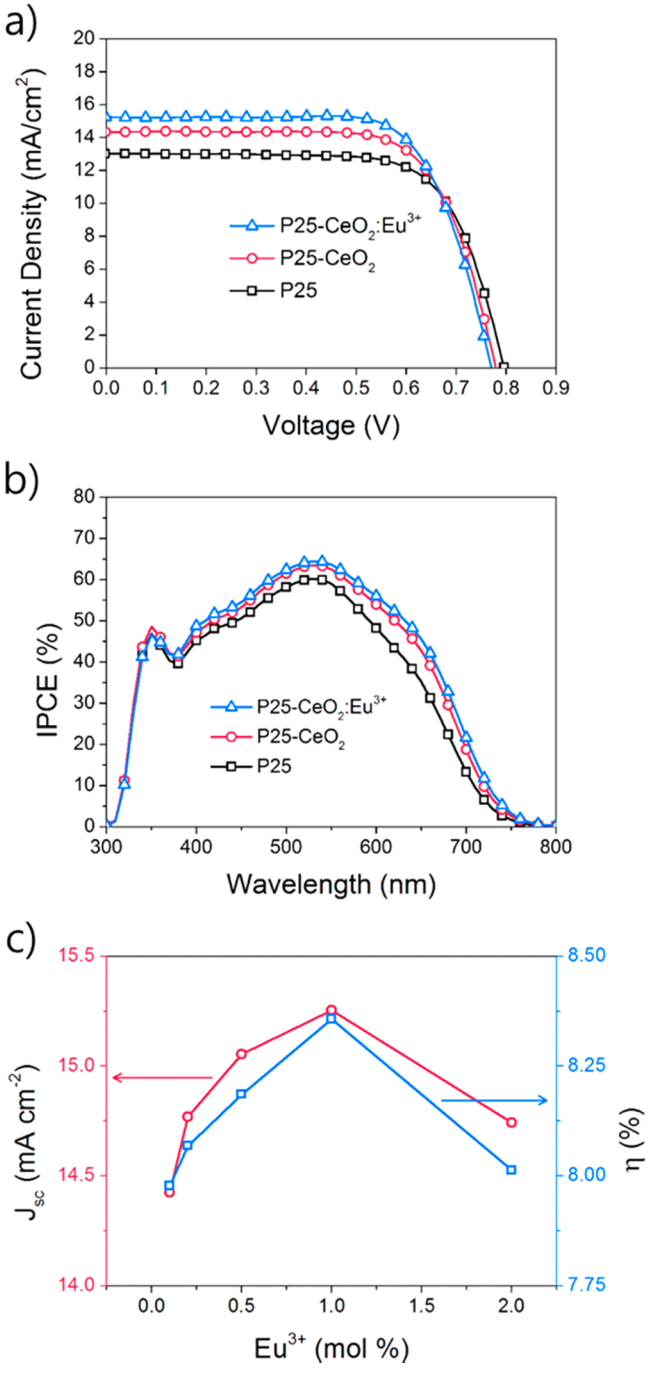

Figure 6. (a) photocurrent density−voltage characteristics (J−V curves), (b) IPCE spectra of downconversion-enhanced DSSCs, and (c) the dependences of J_{sc} and η on the Eu^{3+} concentration of 0.1−2 mol %.

CeO_2:Eu^{3+} nanocrystal also increase. This increased defects may trap photogenerated electrons and cause the recombination of electrons and holes, thus reducing power conversion efficiency.

Figure 6b shows IPCE spectra of the P25, P25-CeO_2, and P25-CeO_2:Eu^{3+} photoanodes. With introducing CeO_2 scattering layer, the IPCE value over the entire region of 400−800 nm was considerably enhanced by excellent light-scattering effect of CeO_2 nanocrystals. The DSSCs with a CeO_2:Eu^{3+} layer exhibits a maximum IPCE value of 64.5% at 530 nm because of downconversion PL of CeO_2:Eu^{3+} nanocrystals. This result is in good agreement with the photovoltaic performance as shown in Figure 6a.

Table 1. Summary of the Photovoltaic Properties of Dye-Sensitized Solar Cells (DSSCs) with Photoanodes Containing CeO_2:Eu^{3+} Nanocrystals (1 mol % Eu^{3+})[a]

sample[b]	thickness (μm)	J_{sc}[c] (mA cm^{-2})	V_{oc}[d] (V)	FF[e]	η[f] (%)	R_{ct} (Ω)
P25	8.06	13.040	0.796	0.706	7.330	2.8
P25-CeO_2	13.08	14.332	0.780	0.709	7.922	3.2
P25-CeO_2:Eu^{3+}	12.98	15.255	0.771	0.711	8.357	3.7

[a]Measurements were performed under AM 1.5G sunlight intensity of 100 mW cm^{-2}. [b]Active area of the assembled DSSC samples is 0.16 cm^2. [c]Short-circuit current. [d]Open-circuit voltage. [e]Fill factor. [f]Power conversion efficiency.

To investigate the charge transfer in assembled DSSCs, EIS measurement was performed under a light intensity of 100 mW cm^{-2}. Figure 7 shows the Nyquist plots of DSSCs with the P25,

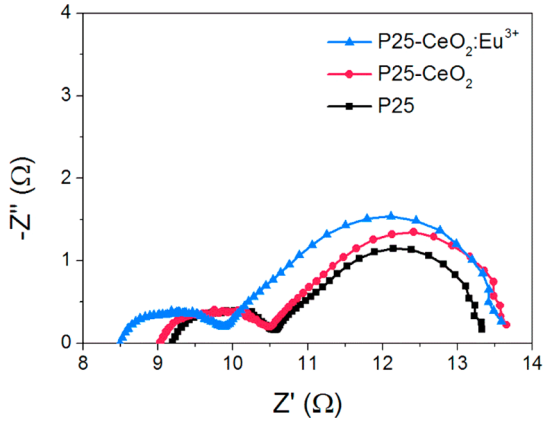

Figure 7. Nyquist plot of downconversion-enhanced DSSCs. EIS measurement was performed under 100 mW cm^{-2}.

P25-CeO_2, and P25-CeO_2:Eu^{3+} photoanodes. The small semicircle at higher frequency range (kHz range) corresponds to the charge transfer at the interfaces of the electrolyte/Pt counter electrode. The large semicircle in the midfrequency region (1−100 Hz) is related to the transport of photoinduced electron at the TiO_2/dye/electrolyte.[47] The resistance values of assembled DSSCs at the TiO_2/dye/electrolyte interface (R_{ct}) are summarized in Table 1. As shown in Figure 7, the R_{ct} values of P25-CeO_2, and P25-CeO_2:Eu^{3+} DSSCs are higher than that of P25 reference cell, implying that inefficient charge transfer occurs in CeO_2 and CeO_2:Eu^{3+} layer. The higher R_{ct} can lead to lower charge transfer, which causes the charge recombination of photoinduced electrons. Considering these results, CeO_2:Eu^{3+} nanocrystals can enhance the power conversion efficiency by remarkable light-scattering and downconversion PL properties. However, the intrinsic defects of CeO_2:Eu^{3+} nanocrystals are not beneficial for the electron transfer, which reduce photocurrent.

CONCLUSION

Octahedral CeO_2:Eu^{3+} nanocrystals, successfully prepared using a simple hydrothermal method, were investigated to determine their photovoltaic properties in DSSCs. The prepared CeO_2:Eu^{3+} nanocrystals were large in size, with mirrorlike facets that provided excellent light-scattering ability. UV light

was converted to visible light via downconversion PL corresponding to the $^5D_0 \rightarrow {}^7F_J$ transitions of trivalent Eu^{3+} ions. By controlling the concentration of Eu^{3+}, the power conversion efficiency of the DSSC with a P25-CeO_2:Eu^{3+} photoanode exhibited the best efficiency of 8.36% at 1 mol % Eu^{3+}, which was an overall 14% enhancement, compared with that of a bare P25 photoanode. This enhanced performance was attributed to the excellent light-scattering and downconversion luminescent properties of CeO_2:Eu^{3+} nanocrystals. With further optimization of CeO_2:Eu^{3+} nanocrystals in DSSCs, it is anticipated that this dual-functional material will provide new opportunities to further enhance light absorption for high-performance DSSCs.

■ ASSOCIATED CONTENT

Supporting Information

SEM images, EDS analysis, photovoltaic properties and $J-V$ curves of CeO_2:Eu^{3+} nanocrystals with increasing Eu^{3+} concentration and the thickness of CeO_2:Eu^{3+} layer. This material is available free of charge via the Internet at http://pubs.acs.org.

■ AUTHOR INFORMATION

Corresponding Author

*E-mail: jsjang@plaza.snu.ac.kr. Tel.: (+82) 2-880-7069. Fax: (+82) 2-888-1604.

Notes

The authors declare no competing financial interest.

■ ACKNOWLEDGMENTS

This work was supported by the Global Frontier R&D Program on the Center for Multiscale Energy System funded by the National Research Foundation under the Ministry of Science, ICT & Future, Korea (2011-0031573).

■ REFERENCES

(1) O'Regan, B.; Gratzel, M. A Low-Cost, High-Efficiency Solar cell Based on Dye-Sensitized Colloidal TiO_2 Films. *Nature* **1991**, *353*, 737−740.
(2) Gratzel, M. Photoelectrochemical Cells. *Nature* **2001**, *414*, 338−344.
(3) Cho, S.; Hwang, S. H.; Kim, C.; Jang, J. Polyaniline Porous Counter-Electrodes for High Performance Dye-Sensitized Solar Cells. *J. Mater. Chem.* **2012**, *22*, 12164−12171.
(4) Grätzel, M. Dye-Sensitized Solar Cells. *J. Photochem. Photobiol., C* **2003**, *4*, 145−153.
(5) Grätzel, M. Solar Energy Conversion by Dye-Sensitized Photovoltaic Cells. *Inorg. Chem.* **2005**, *44*, 6841−6851.
(6) Park, Y.-C.; Chang, Y.-J.; Kum, B.-G.; Kong, E.-H.; Son, J. Y.; Kwon, Y. S.; Park, T.; Jang, H. M. Size-Tunable Mesoporous Spherical TiO_2 as a Scattering Overlayer in High-Performance Dye-Sensitized Solar Cells. *J. Mater. Chem.* **2011**, *21*, 9582−9586.
(7) Hore, S.; Vetter, C.; Kern, R.; Smit, H.; Hinsch, A. Influence of Scattering Layers on Efficiency of Dye-Sensitized Solar cells. *Sol. Energy Mater. Sol. Cells* **2006**, *90*, 1176−1188.
(8) Chen, D.; Huang, F.; Cheng, Y.-B.; Caruso, R. A. Mesoporous Anatase TiO_2 Beads with High Surface Areas and Controllable Pore Sizes: A Superior Candidate for High-Performance Dye-Sensitized Solar Cells. *Adv. Mater.* **2009**, *21*, 2206−2210.
(9) Hagfeldt, A.; Boschloo, G.; Sun, L.; Kloo, L.; Pettersson, H. Dye-Sensitized Solar Cells. *Chem. Rev.* **2010**, *110*, 6595−6663.
(10) Hwang, S. H.; Kim, C.; Song, H.; Son, S.; Jang, J. Designed Architecture of Multiscale Porous TiO_2 Nanofibers for Dye-Sensitized Solar Cells Photoanode. *ACS Appl. Mater. Interfaces* **2012**, *4*, 5287−5292.
(11) Peng, W.; Han, L. Hexagonal TiO_2 Microplates with Superior Light Scattering for Dye-Sensitized Solar Cells. *J. Mater. Chem.* **2012**, *22*, 20773−20777.
(12) Dadgostar, S.; Tajabadi, F.; Taghavinia, N. Mesoporous Submicrometer TiO_2 Hollow Spheres As Scatterers in Dye-Sensitized Solar Cells. *ACS Appl. Mater. Interfaces* **2012**, *4*, 2964−2968.
(13) Huang, F.; Chen, D.; Zhang, X. L.; Caruso, R. A.; Cheng, Y.-B. Dual-Function Scattering Layer of Submicrometer-Sized Mesoporous TiO_2 Beads for High-Efficiency Dye-Sensitized Solar Cells. *Adv. Funct. Mater.* **2010**, *20*, 1301−1305.
(14) Dong, Z.; Lai, X.; Halpert, J. E.; Yang, N.; Yi, L.; Zhai, J.; Wang, D.; Tang, Z.; Jiang, L. Accurate Control of Multishelled ZnO Hollow Microspheres for Dye-Sensitized Solar Cells with High Efficiency. *Adv. Mater.* **2012**, *24*, 1046−1049.
(15) Jiang, W.-T.; Wu, C.-T.; Sung, Y.-H.; Wu, J.-J. Room-Temperature Fast Construction of Outperformed ZnO Nano-architectures on Nanowire-Array Templates for Dye-Sensitized Solar Cells. *ACS Appl. Mater. Interfaces* **2013**, *5*, 911−917.
(16) Qian, J.; Liu, P.; Xiao, Y.; Jiang, Y.; Cao, Y.; Ai, X.; Yang, H. TiO_2-Coated Multilayered SnO_2 Hollow Microspheres for Dye-Sensitized Solar Cells. *Adv. Mater.* **2009**, *21*, 3663−3667.
(17) Li, K.-N.; Wang, Y.-F.; Xu, Y.-F.; Chen, H.-Y.; Su, C.-Y.; Kuang, D.-B. Macroporous SnO_2 Synthesized via a Template-Assisted Reflux Process for Efficient Dye-Sensitized Solar Cells. *ACS Appl. Mater. Interfaces* **2013**, *5*, 5105−5111.
(18) Yu, H.; Bai, Y.; Zong, X.; Tang, F.; Lu, G. Q. M.; Wang, L. Cubic CeO_2 Nanoparticles as Mirror-Like Scattering Layers for Efficient Light Harvesting in Dye-Sensitized Solar Cells. *Chem. Commun.* **2012**, *48*, 7386−7388.
(19) Son, S.; Hwang, S. H.; Kim, C.; Yun, J. Y.; Jang, J. Designed Synthesis of SiO_2/TiO_2 Core/Shell Structure As Light Scattering Material for Highly Efficient Dye-Sensitized Solar Cells. *ACS Appl. Mater. Interfaces* **2013**, *5*, 4815−4820.
(20) Hwang, S. H.; Shin, D. H.; Yun, J.; Kim, C.; Choi, M.; Jang, J. SiO_2/TiO_2 Hollow Nanoparticles Decorated with Ag Nanoparticles: Enhanced Visible Light Absorption and Improved Light Scattering in Dye-Sensitized Solar Cells. *Chem.—Eur. J.* **2014**, *20*, 4439−4446.
(21) Hwang, S. H.; Roh, J.; Jang, J. Nanosilver-Decorated TiO_2 Nanofibers Coated with a SiO_2 Layer for Enhanced Light Scattering and Localized Surface Plasmons in Dye-Sensitized Solar Cells. *Chem.—Eur. J.* **2013**, *19*, 13120−13126.
(22) Khawaja, E. E.; Durrani, S. M. A.; Al-Kuhaili, M. F. Determination of Average Refractive Index of Thin CeO_2 Films with Large Inhomogeneities. *J. Phys. D-Appl. Phys.* **2003**, *36*, 545.
(23) Trupke, T.; Green, M. A.; Würfel, P. Improving Solar Cell Efficiencies by Down-conversion of High-Energy Photons. *J. Appl. Phys.* **2002**, *92*, 1668−1674.
(24) Badescu, V.; Badescu, A. M. Improved Model for Solar Cells with Up-conversion of Low-energy Photons. *Renewable Energy* **2009**, *34*, 1538−1544.
(25) Lee, E.; Ryu, J.; Jang, J. Fabrication of Graphene Quantum Dots via Size-selective Precipitation and Their Application in Upconversion-based DSSCs. *Chem. Commun.* **2013**, *49*, 9995−9997.
(26) Wang, J.; Wu, J.; Lin, J.; Huang, M.; Huang, Y.; Lan, Z.; Xiao, Y.; Yue, G.; Yin, S.; Sato, T. Application of Y_2O_3:Er^{3+} Nanorods in Dye-Sensitized Solar Cells. *ChemSusChem* **2012**, *5*, 1307−1312.
(27) Wu, J.; Wang, J.; Lin, J.; Lan, Z.; Tang, Q.; Huang, M.; Huang, Y.; Fan, L.; Li, Q.; Tang, Z. Enhancement of the Photovoltaic Performance of Dye-Sensitized Solar Cells by Doping $Y_{0.78}Yb_{0.20}Er_{0.02}F_3$ in the Photoanode. *Adv. Energy Mater.* **2012**, *2*, 78−81.
(28) Wu, J.; Wang, J.; Lin, J.; Xiao, Y.; Yue, G.; Huang, M.; Lan, Z.; Huang, Y.; Fan, L.; Yin, S.; Sato, T. Dual Functions of YF_3:Eu^{3+} for Improving Photovoltaic Performance of Dye-Sensitized Solar Cells. *Sci. Rep.* **2013**, *3*, 2058.
(29) Wang, F.; Liu, X. Recent Advances in the Chemistry of Lanthanide-Doped Upconversion Nanocrystals. *Chem. Soc. Rev.* **2009**, *38*, 976−989.

(30) Ovenstone, J.; Titler, P. J.; Withnall, R.; Silver, J. A Study of the Effects of Europium Doping and Calcination on the Luminescence of Titania Phosphor Materials. *J. Phys. Chem. B* **2001**, *105*, 7170−7177.
(31) Wang, J.-W.; Chang, Y.-M.; Chang, H.-C.; Lin, S.-H.; Huang, L. C. L.; Kong, X.-L.; Kang, M.-W. Local Structure Dependence of the Charge Transfer Band in Nanocrystalline Y_2O_3:Eu^{3+}. *Chem. Phys. Lett.* **2005**, *405*, 314−317.
(32) Liu, Y.; Tu, D.; Zhu, H.; Li, R.; Luo, W.; Chen, X. A Strategy to Achieve Efficient Dual-Mode Luminescence of Eu^{3+} in Lanthanides Doped Multifunctional $NaGdF_4$ Nanocrystals. *Adv. Mater.* **2010**, *22*, 3266−3271.
(33) Sankara, R.; Subba Rao, G. V. Eu^{3+} Luminescence, $Ce^{4+} \rightarrow Eu^{3+}$ Energy Transfer, and White-Red Light Generation in Sr_2CeO_4. *J. Electrochem. Soc.* **2000**, *147*, 2773−2779.
(34) Liu, X.; Chen, S.; Wang, X. Synthesis and Photoluminescence of CeO_2:Eu^{3+} Phosphor powders. *J. Lumin.* **2007**, *127*, 650−654.
(35) Fujihara, S.; Oikawa, M. Structure and Luminescent Properties of CeO_2:Rare Earth (RE=Eu^{3+} and Sm^{3+}) Thin Films. *J. Appl. Phys.* **2004**, *95*, 8002−8006.
(36) Oikawa, M.; Fujihara, S. Sol−gel Preparation and Luminescent Properties of CeO_2:Ln (Ln = Eu^{3+} and Sm^{3+}) Thin Films. *J. Eur. Ceram. Soc.* **2005**, *25*, 2921−2924.
(37) Lin, H.; Huang, C. P.; Li, W.; Ni, C.; Shah, S. I.; Tseng, Y.-H. Size Dependency of Nanocrystalline TiO_2 on its Optical Property and Photocatalytic Reactivity Exemplified by 2-chlorophenol. *Appl. Catal., B* **2006**, *68*, 1−11.
(38) Wang, Q.; Moser, J.-E.; Grätzel, M. Electrochemical Impedance Spectroscopic Analysis of Dye-Sensitized Solar Cells. *J. Phys. Chem. B* **2005**, *109*, 14945−14953.
(39) Yan, L.; Yu, R.; Chen, J.; Xing, X. Template-Free Hydrothermal Synthesis of CeO_2 Nano-octahedrons and Nanorods: Investigation of the Morphology Evolution. *Cryst. Growth Des.* **2008**, *8*, 1474−1477.
(40) Liao, X.-H.; Zhu, J.-M.; Zhu, J.-J.; Xu, J.-Z.; Chen, H.-Y. Preparation of Monodispersed Nanocrystalline CeO_2 Powders by Microwave Irradiation. *Chem. Commun.* **2001**, 937−938.
(41) Tsunekawa, S.; Sahara, R.; Kawazoe, Y.; Ishikawa, K. Lattice Relaxation of Monosize CeO_{2-x} Nanocrystalline Particles. *Appl. Surf. Sci.* **1999**, *152*, 53−56.
(42) Zhang, H.; Han, Y.; Liu, X.; Liu, P.; Yu, H.; Zhang, S.; Yao, X.; Zhao, H. Anatase TiO_2 Microspheres with Exposed Mirror-like Plane {001} Facets for High Performance Dye-Sensitized Solar Cells (DSSCs). *Chem. Commun.* **2010**, *46*, 8395−8397.
(43) Kenyon, A. J. Recent Developments in Rare-Earth Doped Materials for Optoelectronics. *Prog. Quantum Electron.* **2002**, *26*, 225−284.
(44) Stouwdam, J. W.; van Veggel, F. C. J. M. Near-infrared Emission of Redispersible Er^{3+}, Nd^{3+}, and Ho^{3+} Doped LaF_3 Nanoparticles. *Nano Lett.* **2002**, *2*, 733−737.
(45) Kuang, D.; Ito, S.; Wenger, B.; Klein, C.; Moser, J.-E.; Humphry-Baker, R.; Zakeeruddin, S. M.; Grätzel, M. High Molar Extinction Coefficient Heteroleptic Ruthenium Complexes for Thin Film Dye-Sensitized Solar Cells. *J. Am. Chem. Soc.* **2006**, *128*, 4146−4154.
(46) Kydd, R.; Scott, J.; Teoh, W. Y.; Chiang, K.; Amal, R. Understanding Photocatalytic Metallization of Preadsorbed Ionic Gold on Titania, Ceria, and Zirconia. *Langmuir* **2009**, *26*, 2099−2106.
(47) van de Lagemaat, J.; Park, N. G.; Frank, A. J. Influence of Electrical Potential Distribution, Charge Transport, and Recombination on the Photopotential and Photocurrent Conversion Efficiency of Dye-Sensitized Nanocrystalline TiO_2 Solar Cells: A Study by Electrical Impedance and Optical Modulation Techniques. *J. Phys. Chem. B* **2000**, *104*, 2044−2052.